Design and Analysis of an Improved Tubular Permanent Magnet Linear Machine with a T-type Magnet Array

Rong Guo, *Member IEEE*, Yanan Bian, Baocheng Guo , *Member IEEE*, Fengyu Zhang, *Member IEEE*, Wenna Wang

***Abstract*—The surface-mounted tubular permanent magnet linear machine (SM-TPMLM) is widely used in many industrial applications. However, the PMs are fragile and easily fall off when linear machines are operated at reciprocating oscillation speed over long periods or encounter harsh environments, the exposed PMs are susceptible to corrosion, which reduces the service life of linear machines. To solve this problem, an improved tubular permanent magnet linear machine with a T-type magnet array (T-TPMLM) is proposed. The axial and radial magnets are combined in a magnetic pole array to increase the thrust force, power and protect the PMs. First, an equivalent analytical model of T-TPMLM is established to predict the magnetic field, the subdomain method with Schwarz-Christoffel mapping method is introduced to consider slotting effect and end effect. Then, to verify the merit of the proposed T-TPMLM, a quantitative electromagnetic performance comparison with two traditional SM-TPMLM including radial magnetization and Halbach magnetization is performed through the finite element analysis method (FEM). Besides, the mechanical strength of three linear machines is discussed briefly. Finally, a prototype of proposed T-TPMLM is manufactured and tested to validate the effectiveness of the analytical model and the FEA predicted results. The results show that the proposed machine offers high electromagnetic performance.**

***Index Terms*—tubular permanent magnet linear machine, T-type magnet array, magnetic field, subdomain method.**

I. Introduction

Permanent magnet linear machines (PMLMs) have the advantages of a simple structure, high reliability, less energy loss and are widely used in the transportation, high-precision manufacturing and aerospace fields [1]–[3]. To achieve high thrust and power density, the magnetic array of PMLMs has been further studied. According to the different magnetization arrangements of the PMs, the PMLM mechanism can be mainly classified as using radial magnetization, axial magnetization and Halbach magnetization [4]–[6]. With the development of electromagnetic technology, various analytical methods have been reported to calculate the magnetic field, which plays an important role in the intensive study of PMLM output performance [7]–[9].

Conventional radial magnetization arrangements have received great attention in PMLM for their simple structure and easy assembly [9]–[13]. In [10], a novel analytical model is presented based on the subdomain method to predict the magnetic field in a PMLM. A PM model with radial magnetization is established that can consider end effects. Then, based on the Maxwell stress theory, the thrust and normal forces are calculated. The analytical results are validated by tests and the finite element (FE) method, and the proposed analytical model is found to be highly accurate. In [11], a double-sided PMLSM structure with an end slot reversed structure is proposed to minimize the cogging force, which is the interaction between the slots and the PMs. The PMs are mounted on both sides of the back iron with radial alternating magnetization. The Fourier series method is used to calculate the cogging force. In addition, to address the unbalanced back electromotive force (EMF) caused by the reversed slot, two novel windings are added. According to this topology structure, a 9-slot 8-pole prototype is manufactured and tested, and the results show that the proposed structure is very effective in reducing the cogging force. In [12], a single-phase tubular permanent magnet motor is analysed by a design methodology that can consider the steady-state characteristics, and the iron loss is calculated based on an analytical formula. Moreover, the influence of compressor loads on rated operating conditions is evaluated through a design procedure. The analysis results are verified by experiments, and the results show that by optimizing two leading dimensional ratios, the motor efficiency can be improved.

Compared with radial magnetizations, axially magnetized PMs can provide high flux density and power density [14]–[18]. In [14], a single-phased linear oscillating actuator (LOA) with axially magnetized shape magnets is designed for use in refrigerator compressors. The topological structure is described in detail. The PMs are placed along the z-axis in opposite directions, and the mover core lies between the two PMs. To obtain the best parameters of LOA, the FEM parametric sweep method is used for analysis. The results show that the proposed structure has a large thrust force density with low-cost PMs. In [15] [16], TLSMs with axially magnetized PMs are studied, an optimum flux passing iron pole design is presented, and a magnetic circuit is established that considered the leakage flux. Then, to improve the initial design time, the subdomain method is used to analyse the tubular linear synchronous machine (TLSM), the analytical solution of each region is derived based on boundary

This work was supported in part by the National Nature Science Foundation of China under Grant 51907027, and in part by R&D Program of Beijing Municipal Education Commission (KM202310016005), and in part by BUCEA Young Scholar Research Capability Improvement Plan under Grant X21081. (*Corresponding author*: *Rong Guo*.)

Rong Guo, Yanan Bian and Wenna Wang are with the School of Electrical and information engineering, Beijing University of Civil Engineering and Architecture, Beijing, 102616, China. (e-mail: 18813189123@163.com; 15709323789@163.com; outlier050404@qq.com)

Baocheng Guo is with School of Electrical and Automation Engineering Nanjing Normal University, Nanjing, 210046, China. (e-mail: guobaocheng1986@gmail.com)

Fengyu Zhang is with the Power Electronics Machines and Control (PEMC) Research Group, University of Nottingham, Nottingham, NG7 2RD, UK. (e-mail: fengyu.zhang@nottingham.ac.uk)

conditions, and the electromagnetic performance is predicted. The nonlinear FE method and prototype machine are used to verify the proposed method. In [18], an improved axially magnetized tubular permanent magnet (TPM) machine is proposed, and annular shape magnets are used and supported by a nonferromagnetic rod. The advantage of this structure is that it not only decreases the effective gap but also reduces the moving mass. Furthermore, an analytical model is established to predict the magnetic field distribution, and the EMF and force ripple are calculated. The results are validated by the FEM, which shows that the proposed linear machine has a higher force capability, and the analytical model results are in good agreement with the FE results.

Halbach magnet arrays can be regarded as a combination of radial magnetization and axial magnetization, with the advantage of enhanced magnetic field intensity [19]–[23]. In [19], a novel ironless tubular linear machine with a Halbach array is analysed and designed. The magnetization expression of the magnet array is derived, and the magnetic field is calculated based on the harmonic function method. This proposed motor is tested in a machine tool application to confirm its efficacy. In [22], a segmented Halbach array permanent magnet machine is studied by an analytical model. The B-H curve and saturation effect are both considered. The iron permeability variation is calculated based on the Cauchy product theorem and an iterative algorithm. The analytical results are compared with FEM and prototype results, showing that the analytical model is suitable for any number segmented magnets design. In [23], a dual Halbach-array tubular linear motor is proposed that is able to improve the large axial force. In this topological structure, the stator yoke is omitted, and the set of teeth is magnetically separated. The semi-analytical model and 3D FE method are used to design the performance of the linear machine.

For the above research, the surface-mounted radial magnetizing structure is simple, however, for special applications such as high-frequency oscillation and wave power generation etc., the permanent magnet is fragile and its magnetic circuit is heavily dependent on the back mounting, which is not conducive to lightweight design of the mover. Axial and Halbach magnetizing structures can produce large magnetic flux density, but there are certain difficulties in pole assembly, especially for tubular permanent magnet linear machines. Therefore, in this paper, an improved tubular permanent magnet linear machine with a T-type PM structure is proposed and analysed. The mover is made up of embedded PMs with a radial magnetization in conjunction with an axial magnetized array, which has the advantages of a high thrust force, low magnetic flux leakage, good self-shielding and easy maintenance. The paper is organized as follows: Section II introduces the structure and principle of the T-type TPMLM. Based on the structure, an equivalent analysis model of the magnetic field is established using the subdomain (SD) method, the general solution of each region is given, and according to the magnetic field analysis results, the back-EMF and thrust force are calculated in Section III. In Section V, the overall comparison of two linear machine using FEM are conducted, and experiments are adopted to validate the proposed linear machine. The conclusions of the research are summarized at the end of the paper.

II. Structure of the Proposed T-TPMLM

The proposed structure of the T-TPMLM is shown in Fig. 1. In primary stator iron, fractional slot concentrated winding and auxiliary teeth are used, which have the advantages of a low detent force, high efficiency, and no end winding. The secondary mover consists of two types of PMs: embedded PMs with a radial magnetization array and an axial magnet array. This PM structure can be equivalent to two layers, i.e., an outer layer with a segment Halbach magnet array and an inner layer with a conventional axial magnet array. The main function of the outer layer is to concentrate the magnetic flux and enhance the thrust force, and the inner layer suppresses flux leakage.

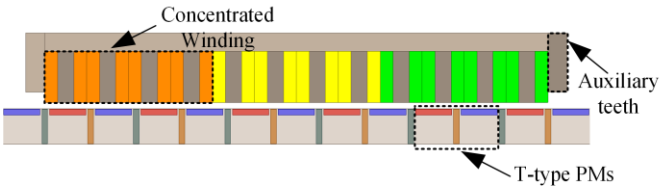

Fig. 1. Proposed structure of the T-TPMLM

Since fractional slot concentrated winding is adopted, phase division should be carried out according to the winding vector diagram, as shown in Fig. 2. The current distribution of the T-TPMLM is shown in Fig. 3.

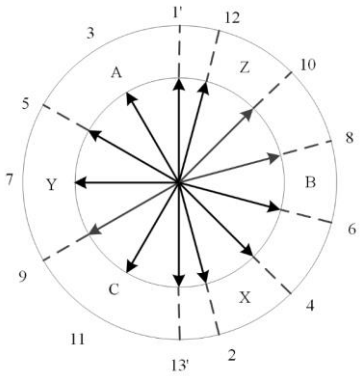

Fig. 2. Diagram vector of the winding EMF

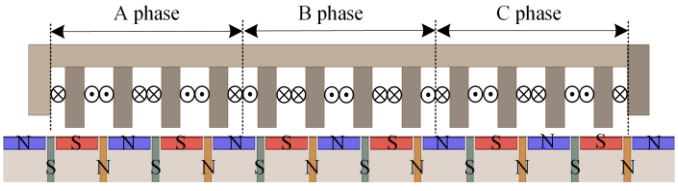

Fig. 3. Current distribution of the T-TPMLM

To explain the proposed machine operating principle, the distribution of the main magnetic flux path is demonstrated in Fig. 4(a). The T-TPMLM mainly includes three magnetic circuits, φ_1 is formed by a radially magnetized permanent magnet, φ_2 is produced by the interaction of radial and tangentially magnetized permanent magnets and φ_3 is generated by the tangentially magnetized permanent magnets. The flux comes from radially magnetized PM, crosses the air gap to teeth and yoke, then returned from the tangentially

magnetized PM. By analysing the composition of the magnetic circuits, the proposed array has the effect of flux enhancement, which will be contribute to force improvement. And based on the minimum reluctance principle, the operation process of one phase under one pole pair is shown in Fig. 4(b)-(d). When the mover is in the initial position x=0, the magnetic flux of the coil hinge is the largest as shown in Fig. 4(b), with the mover to $x=\tau_p/2$ (τ_p is pole-pitch), the magnetic flux on tooth 2 and 3 is located in the local area which does not cross-link with the coil, meanwhile the coil polarity on tooth 1 and 4 is anti-series, so the flux linkage is zero. Finally, when the mover to $x=\tau_p$, the magnetic flux reaches the maximum reverse. Therefore, with the magnetic flux changes, the EMF and force will be generated in the T-TPMLM.

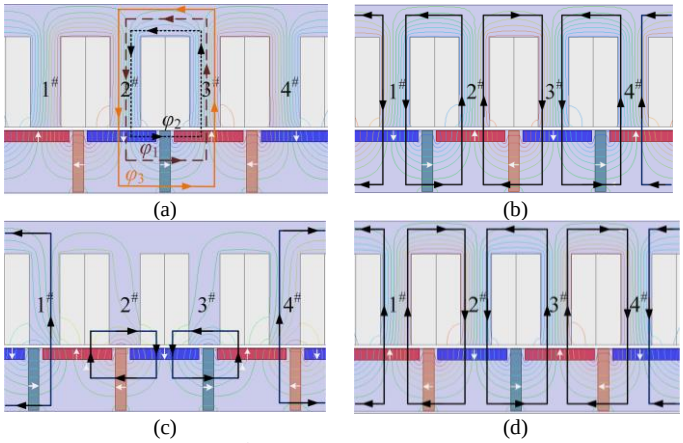

Fig. 4 Operation principle of the T-TPMLM
(a) Diagram of flux path under the open-circuit condition
(b) Flux path of T-TPMLM at x=0
(c) Flux path of T-TPMLM at $x=\tau_p/2$
(d) Flux path of T-TPMLM at $x=\tau_p$

III. Magnetic Field Analysis Model of the T-TPMLM

The accuracy of the magnetic field calculation directly affects the output performance of the linear machine. Considering that the FEA method is time-consuming in the initial design, the analytical method is adopted to design and analyse the T-TPMLM.

A. *No-load condition of the magnetic field*

Under no-load conditions, a magnetic field is generated by PMs, in this paper, the T-type PM analysis model can be equated as shown in Fig. 5. The PM is separated into two parts: 1) quasi-Halbach magnetized and 2) axially magnetized.

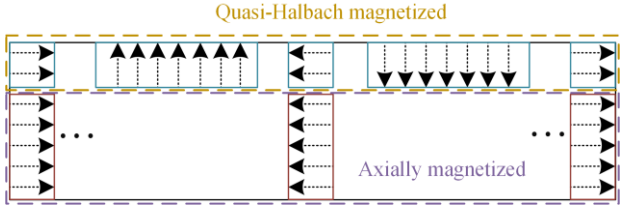

Fig. 5 Analysis of the equivalent model of the T-type PM

In the cylindrical coordinate system, the magnetization $\boldsymbol{M}$ is made up of radial and axial components, which is expressed as

$$\overrightarrow{M} = M_r \cdot \overrightarrow{e_r} + M_z \cdot \overrightarrow{e_z} \tag{1}$$

where M_r is the radial component of $\boldsymbol{M}$ and M_z is the axial component of $\boldsymbol{M}$.

The distributions of M_r and M_z are given in Fig. 6. The Fourier series expansion of $\boldsymbol{M}$ is based on [24]

$$\begin{cases} M_r(z) = \sum_{n=1}^{\infty} M_{rn} \cos(m_n z) \\ M_z(z) = \sum_{n=1}^{\infty} M_{zn} \sin(m_n z) \end{cases} \tag{2}$$

where

$$m_n = n\pi / k\tau_p$$

$$M_{rn} = -\frac{2B_r}{u_0 n\pi}\{\sin(\frac{m_n \tau_{mr}}{2}) + \sin(m_n(\tau_p - \frac{\tau_{mr}}{2})) - \sin(m_n \tau_p)\}$$

$$M_{zn} = -\frac{4B_r}{u_0 n\pi} \sin\frac{m_n \tau_p}{2} \sin\frac{m_n \tau_{mz}}{2}$$

where k is a positive integer, τ_p is the pole-pitch of the PM, τ_{mr} is the width of a radially magnetized PM and τ_{mz} is the width of the axial magnetization of the PM.

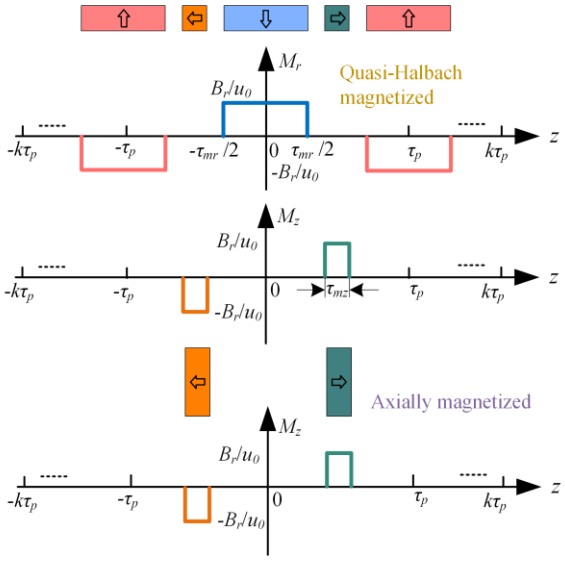

Fig. 6 Distribution of the magnetization $\boldsymbol{M}$

To simplify the calculation complexity, the following assumptions are made, as stated in [24][25]:

1) The magnetic permeability in magnets is a constant u_r.

2) The iron permeability of the stator and mover is infinite; the saturation effect is ignored.

3) The magnetic field distribution is axially symmetric in the z-direction, and the slot effect is considered by Schwarz-Christoffel (SC) conformal mapping.

Based on these assumptions, a simplified analysis model of the T-TPMLM is established, as shown in Fig. 7. The solution fields are divided into 6 regions: 1) inner-air area; 2) axial magnetization area; 3) virtual gap area; 4) quasi-Halbach magnetization area; 5) air-gap area; and 6) end area. It should be note that considering the boundary complexity at the junction of axial and Halbach magnetization, the virtual air region is added to easy modelling process, when calculating this region, the radius of the corresponding area can be taken to a minimum value.

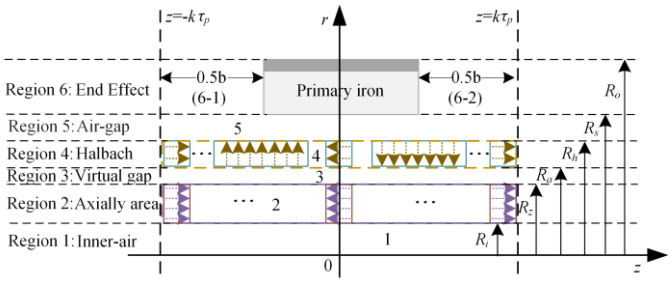

Fig. 7 Simplified analysis model of the T-TPMLM

To determine the magnetic flux density in each region, the vector potential $\boldsymbol{A}$ is introduced, which is governed by the Poisson equation and Laplace equation as follows:

$$\frac{\partial}{\partial z}(\frac{1}{r}\frac{\partial}{\partial z}(rA_{\theta i}))+\frac{\partial}{\partial r}(\frac{1}{r}\frac{\partial}{\partial r}(rA_{\theta i}))=\sum_{n=1}^{\infty}P_n\sin m_n z \quad (i=2,4) \tag{3}$$

$$\frac{\partial}{\partial z}(\frac{1}{r}\frac{\partial}{\partial z}(rA_{\theta i}))+\frac{\partial}{\partial r}(\frac{1}{r}\frac{\partial}{\partial r}(rA_{\theta i}))=0 \quad (i=1,3,5,6) \tag{4}$$

where

$$P_n=\frac{2B_r}{\tau_p}[\sin(m_n\frac{\tau_{mr}}{2})-\sin(m_n(\tau_p+\frac{\tau_{mr}}{2}))+\sin(m_n\tau_p)]$$

By using the variable separation approach, the general solution of the flux density in each area can be derived as follows:

Region 1 (inner-air area):

$$B_{1r}(r,z)=\sum_{n=1}^{\infty}[a_{1n}BI_1(m_n r)]\sin(m_n z) \tag{5}$$

$$B_{1z}(r,z)=\sum_{n=1}^{\infty}[a_{1n}BI_0(m_n r)]\cos(m_n z) \tag{6}$$

Region 2 (axial magnetization area):

$$B_{2r}(r,z)=\sum_{n=1}^{\infty}\left\{\begin{matrix}[F_{An}(m_n r)+a_{2n}]BI_1(m_n r)\\ +[-F_{Bn}(m_n r)+b_{2n}]BK_1(m_n r)\end{matrix}\right\}\sin(m_n z) \tag{7}$$

$$B_{2z}(r,z)=\sum_{n=1}^{\infty}\left\{\begin{matrix}[F_{An}(m_n r)+a_{2n}]BI_0(m_n r)\\ -[-F_{Bn}(m_n r)+b_{2n}]BK_0(m_n r)\end{matrix}\right\}\cos(m_n z) \tag{8}$$

where $F_{An}(m_n r)$ and $F_{Bn}(m_n r)$ are given by

$$\begin{cases}F_{An}(m_n r)=\dfrac{P_n}{m_n}\displaystyle\int_{m_n R_z}^{m_n r}\frac{BK_1(x)}{BI_1(x)BK_0(x)+BK_1(x)BI_0(x)}dx\\ F_{Bn}(m_n r)=\dfrac{P_n}{m_n}\displaystyle\int_{m_n R_z}^{m_n r}\frac{BI_1(x)}{BI_1(x)BK_0(x)+BK_1(x)BI_0(x)}dx\end{cases}$$

Region 3 (virtual gap area):

$$B_{3r}(r,z)=\sum_{n=1}^{\infty}[a_{3n}BI_1(m_n r)+b_{3n}BK_1(m_n r)]\sin(m_n z) \tag{9}$$

$$B_{3z}(r,z)=\sum_{n=1}^{\infty}[a_{3n}BI_0(m_n r)-b_{3n}BK_0(m_n r)]\cos(m_n z) \tag{10}$$

Region 4 (quasi-Halbach magnetization area):

$$B_{4r}(r,z)=\sum_{j=1}^{\infty}[a_{4j}BI_1(q_j r)+b_{4j}BK_1(q_j r)]\sin(q_j z) \tag{11}$$

$$B_{4z}(r,z)=\sum_{j=1}^{\infty}[a_{4j}BI_0(q_j r)-b_{4j}BK_0(q_j r)]\cos(q_j z)+B_0 \tag{12}$$

where $q_j=2\pi j/\tau_{mz}$ and B_0 is shown in [18].

Region 5 (air-gap area):

$$B_{5r}(r,z)=\sum_{n=1}^{\infty}[a_{5n}BI_1(m_n r)+b_{5n}BK_1(m_n r)]\sin(m_n z) \tag{13}$$

$$B_{5z}(r,z)=\sum_{n=1}^{\infty}[a_{5n}BI_0(m_n r)-b_{5n}BK_0(m_n r)]\cos(m_n z) \tag{14}$$

Region 6 (end area):

$$B_{6r}(r,z)=\sum_{s=1}^{\infty}[a_{6s}BI_1(m_s r)+b_{6s}BK_1(m_s r)]\sin m_s(z-z_s) \tag{15}$$

$$B_{6r}(r,z)=\sum_{s=1}^{\infty}[a_{6s}BI_0(m_s r)+b_{6s}BK_0(m_s r)]\cos m_s(z-z_s) \tag{16}$$

where $m_s=s\pi/b$, $z_s=k\tau_p-b/2$, s is a positive integer, and b is the virtual slot width at the end of the T-TPMLM. BI_0 and BI_1 are the first kind of modified Bessel functions, and BK_0 and BK_1 are the second kind of modified Bessel functions. In addition, a_{1n}, a_{2n}, b_{2n}, a_{3n}, b_{3n}, a_{4j}, b_{4j}, a_{5n}, b_{5n}, a_{6s}, and b_{6s} are unknown coefficients.

To solve the foregoing unknown coefficients, the boundary conditions and interface conditions are introduced as follows:

$$\begin{cases}B_{1r}\big|_{r=R_i}=B_{2r}\big|_{r=R_i}\\ H_{1z}\big|_{r=R_i}=H_{2z}\big|_{r=R_i}\end{cases} \quad z\in(-\tau_{mz}/2,\tau_{mz}/2) \tag{17}$$

$$\begin{cases}B_{2r}\big|_{r=R_z}=B_{3r}\big|_{r=R_z}\\ H_{2z}\big|_{r=R_z}=H_{3z}\big|_{r=R_z}\end{cases} \quad z\in(-\tau_{mz}/2,\tau_{mz}/2) \tag{18}$$

$$\begin{cases}B_{4r}\big|_{r=R_a}=B_{3r}\big|_{r=R_a}\\ H_{4z}\big|_{r=R_a}=H_{3z}\big|_{r=R_a}\end{cases} \quad z\in(-\tau_{mz}/2,\tau_{mz}/2)\cup(-\tau_{mr}/2,\tau_{mr}/2) \tag{19}$$

$$\begin{cases}B_{4r}\big|_{r=R_h}=B_{5r}\big|_{r=R_h}\\ H_{4z}\big|_{r=R_h}=H_{5z}\big|_{r=R_h}\end{cases} \quad z\in(-\tau_{mz}/2,\tau_{mz}/2)\cup(-\tau_{mr}/2,\tau_{mr}/2) \tag{20}$$

$$\begin{cases}B_{6r}\big|_{r=R_s}=B_{5r}\big|_{r=R_s}\\ H_{6z}\big|_{r=R_s}=H_{5z}\big|_{r=R_s}\end{cases} \quad z\in(k\tau_p-s/2,k\tau_p+s/2) \tag{21}$$

$$\int_{R_i}^{R_z}rB_{2z}(r,\frac{\tau_{mr}}{2})dr=\int_{\tau_{mr}/2}^{\tau_p/2}\{R_hB_{3r}(R_h,z)-R_iB_{2r}(R_i,z)\}dz \tag{22}$$

By combining the general solution equations with the above boundary conditions, the unknown coefficients in each subdomain region can be found. The specific derivation process follows that of [25], [27] and [28].

To consider the slot effect, the SC mapping method is carried out, as shown in Fig. 8. A slotted air gap plane can be transformed into a slotless air gap plane via a two-step transformation process.

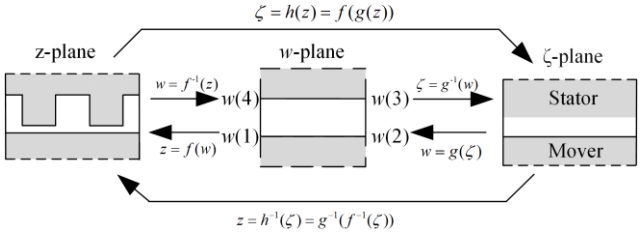

Fig. 8. Transformation process of the SC mapping method

The mapping function from the *w*-plane to the *z*-plane using SC mapping is given by:

$$z = f(w) = A + C\int \prod_{k=1}^{q-1}(w - w_k)^{-a_k/\pi} dw \tag{23}$$

where A and C represent the complex integration coefficients, q represents the number of polygon vertices in the -plane, w is the number of points in the canonical domains, and a_k represents the interior angles. All the above parameters can be obtained from the SC Toolbox.

The mapping the ζ -plane to a rectangular domain in the w-plane is expressed as follows:

$$w = g(\zeta) = j(\log(\zeta)\frac{\Delta x}{2\pi} + \frac{\Delta y}{2} - j\frac{\Delta x}{2}) \tag{24}$$

where

$$\begin{cases} \Delta x = Real[w(1)] - Real[w(4)] \\ \Delta y = Imag[w(2)] - Imag[w(1)] \end{cases}$$

Finally, the flux density in the slot region can be derived using the following equations:

$$B_s = B_g \cdot \lambda = (B_r + j \cdot B_t) \cdot (\lambda_r + j\lambda_t) \tag{25}$$

where B_g is the slotless air-gap flux density in the subdomain model and B_r and B_t are the radial and tangential components under open circuit conditions, respectively.

In this paper, considering the particular structure of the T-TPMLM, the slot effect includes two parts: the whole slot and the new slot caused by auxiliary teeth. To comprehensively consider the above effects, the diagram in Fig. 9 is used for calculation.

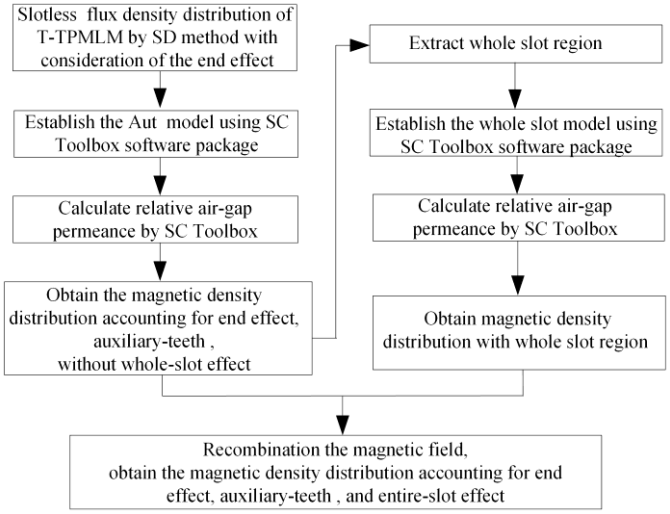

Fig. 9. Calculation diagram illustration of the slot effect

B. *Armature reaction of the magnetic field*

The armature reaction magnetic field is mainly generated by coils, and the current distribution in fractional slot concentrated winding can be predicted using the current sheet model [27]. According to Ampere's law, the ampere turn current in a slot can be equivalent to a current sheet N_cI/b_s distributed over the width of the slot opening b_s at the armature radius R_s. The equivalent current sheet distribution is shown in Fig. 10.

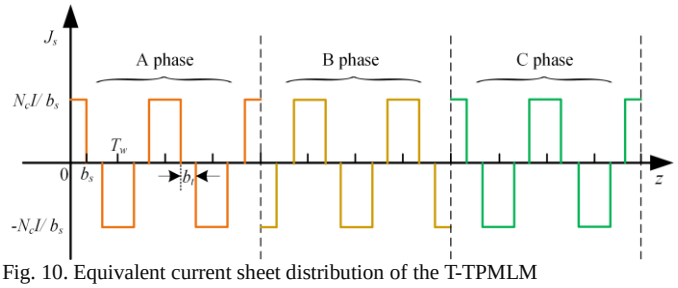

Fig. 10. Equivalent current sheet distribution of the T-TPMLM

From Fig. 10, the current distribution can be expanded into a Fourier series in the following form:

$$J_s(z) = \sum_{n=1}^{\infty} J_n \sin m_{an} z \tag{26}$$

where $m_{an}=n\pi/\tau_{mp}$, τ_{mp} represents the length of the stator, and J_n can be calculated by

$$J_n = \frac{1}{\tau_{mp}} \int_{-\tau_{mp}}^{\tau_{mp}} J_{s(z)} \sin m_{an} z dz \tag{27}$$

The current density distribution for three-phase winding is given by:

$$\begin{aligned} J_A &= -\frac{J_a}{n\pi}(-1)^{i_a}[\cos m_{an}(i_a T_w + b_s) - \cos m_{an}(i_a T_w)] \\ &-\frac{J_a}{n\pi}(-1)^{i_a+1}[\cos(m_{an}(i_a+1)T_w) - \cos(m_{an}(i_a T_w + b_s + b_t))] \end{aligned} \tag{28}$$

where i_a = 0,1,2,……N_s/3-1 and N_s represents the number of slots.

$$\begin{aligned} J_B &= -\frac{J_b}{n\pi}(-1)^{i_b+1}[\cos m_{an}(i_b T_w + b_s) - \cos m_{an}(i_b T_w)] \\ &-\frac{J_b}{n\pi}(-1)^{i_b}[\cos(m_{an}(i_b+1)T_w) - \cos(m_{an}(i_b T_w + b_s + b_t))] \end{aligned} \tag{29}$$

where $i_b = N_s/3, N_s/3+1,\cdots\cdots 2N_s/3-1$.

$$\begin{aligned} J_c &= -\frac{J_c}{n\pi}(-1)^{i_c}[\cos m_{an}(i_c T_w + b_s) - \cos m_{an}(i_c T_w)] \\ &-\frac{J_c}{n\pi}(-1)^{i_c+1}[\cos(m_{an}(i_c+1)T_w) - \cos(m_{an}(i_c T_w + b_s + b_t))] \end{aligned} \tag{30}$$

where $i_c = 2/3N_s, 2N_s/3+1,\cdots\cdots N_s-1$.

Then,

$$J_n = \frac{2}{\tau_{mp}}(J_A + J_B + J_c) \tag{31}$$

To obtain the analytical solution of the armature reaction field, the permeability of PM is assumed to be equal to air, and the solution regions can be simplified to coil region I and unmagnetized PM region II. The armature reaction field model is shown in Fig. 11.

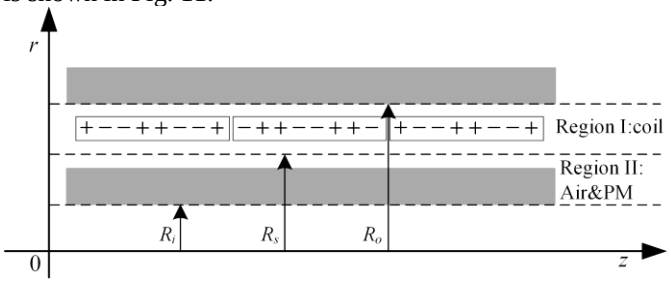

Fig. 11. Armature reaction field model of the T-TPMLM

For each region, the governing equation for the armature reaction field is given by

$$\frac{\partial}{\partial z}\left(\frac{1}{r}\frac{\partial}{\partial z}(rA_{\theta 1})\right)+\frac{\partial}{\partial r}\left(\frac{1}{r}\frac{\partial}{\partial r}(rA_{\theta 1})\right)=-u_0\overrightarrow{J_s} \tag{32}$$

$$\frac{\partial}{\partial z}\left(\frac{1}{r}\frac{\partial}{\partial z}(rA_{\theta 1})\right)+\frac{\partial}{\partial r}\left(\frac{1}{r}\frac{\partial}{\partial r}(rA_{\theta 1})\right)=0 \tag{33}$$

The corresponding generation solution is obtained as:

$$B_r(r,z)=-\sum_{n=1}^{\infty}[a_{na}BI_1(m_{an}r)\cos(m_{an}z)] \tag{34}$$

$$B_z(r,z)=\sum_{n=1}^{\infty}[a_{na}BI_0(m_{an}r)\sin(m_{an}z)] \tag{35}$$

where $a_{na}=u_0J_n\big/BI_0(m_{an}R_s)$

According to the following boundary conditions, the flux density solution of the armature reaction field can be derived.

$$B_z\big|_{r=R_s}=u_0J_s(z) \tag{36}$$

$$B_r\big|_{r=R_i}=0 \tag{37}$$

C. Calculation of the EMF and thrust force

To predict the EMF of the T-TPMLM, the coil flux linkage needs to be calculated as stated in [26], and the integration formula is given by:

$$\psi_w=\frac{N_c}{2b_s(R_o-R_s)}\int_{z-b_s}^{z+b_s}\int_{R_s}^{R_o}2\pi rA_{r3}(r,z)drdz \tag{38}$$

where N_c represent the number of coils.

Based on the flux linkage, the EMF can be calculated using (30)

$$E_a=-\frac{\partial\psi_w}{\partial t}=-\frac{\partial\psi_w}{\partial\Delta_z}\frac{\partial\Delta_z}{\partial t}=-v_m\frac{\partial\psi_w}{\partial\Delta_z} \tag{39}$$

where v_m represents the mover speed of the T-TPMLM.

The thrust force of one coil can be analysed based on the air-gap flux density, which is derived as

$$F_t=\int_{z-b_s}^{z+b_s}\int_{R_s}^{R_o}2\pi rJB_{r3}(r,z)drdz \tag{40}$$

The thrust of the entire linear machine can be obtained by adding up the forces generated by each coil.

IV. Comparison with the FEM and Validation by Experiment

To verify the foregoing analytical model, the FEA method and experiments are conducted with the T-TPMLM, and the distribution of magnetic flux at two typical positions is shown in Fig. 12. The flux lines stream from the PM to the stator and back to the PM to form a complete magnetic flux cycle. When the flux line flows through the PM, the T-type PM arrays can effectively reduce leakage and provide good magnetization effect, which improves the output performance of the linear machine.

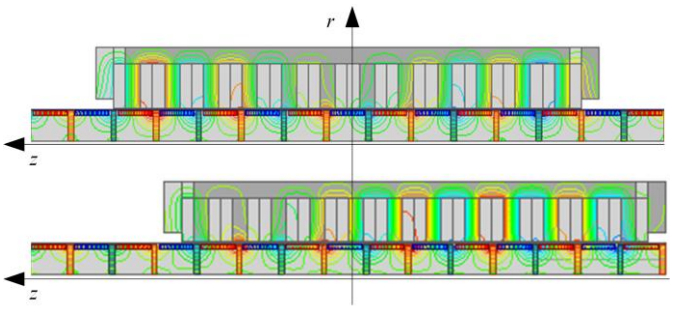

Fig. 12. Magnetic flux distribution of the T-TPMLM at two typical positions

A. Analysis method verified by FEA method

Figs. 13 and 14 show the results of the comparison between the analytical and FEA methods for the slotless air-gap magnetic flux density distribution when the mover is located at the middle and end positions. The SD analytical results coincide well with the FEM predictions, which illustrates that the SD method can accurately account for the end effects of the T-TPMLM. Fig. 13 clearly shows that the radial magnetic flux density in the end region is smaller than that in the iron area, and the value varies from -0.46 T to 0.46 T, while the tangential magnetic density distribution in Fig. 14 is opposite, the end region is higher than the iron area, and the value is approximately 0.62 T.

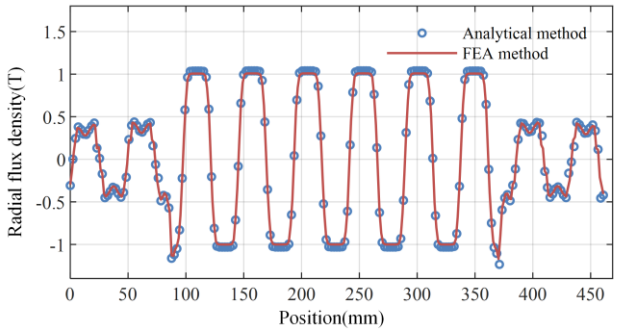

(a)

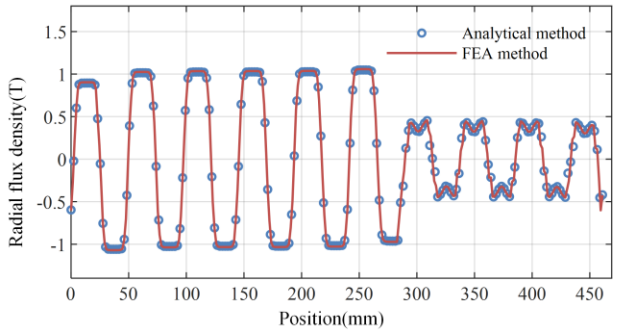

(b)

Fig. 13. Radial magnetic density distribution of the T-TPMLM at two typical positions
(a) Radial magnetic density distribution at the middle position
(b) Radial magnetic density distribution at the end position

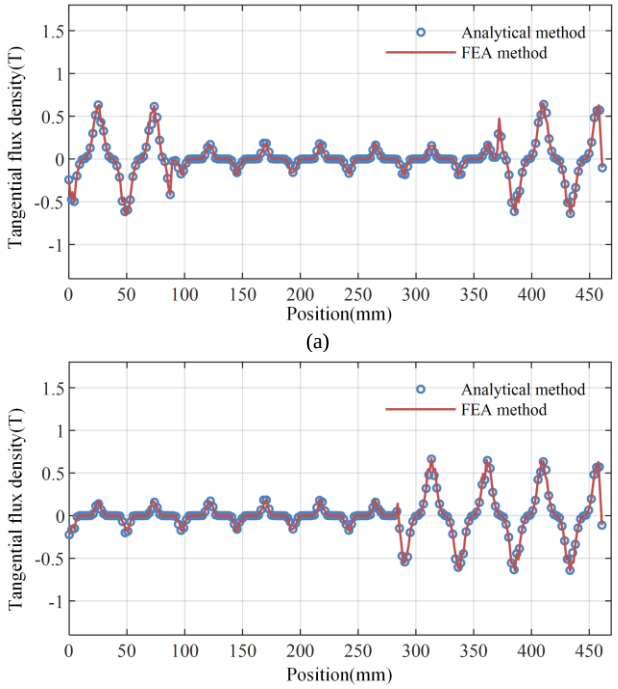

Fig. 14. Tangential magnetic density distribution of the T-TPMLM at two typical positions
(a) Tangential magnetic density distribution at the middle position
(b) Tangential magnetic density distribution at the end position

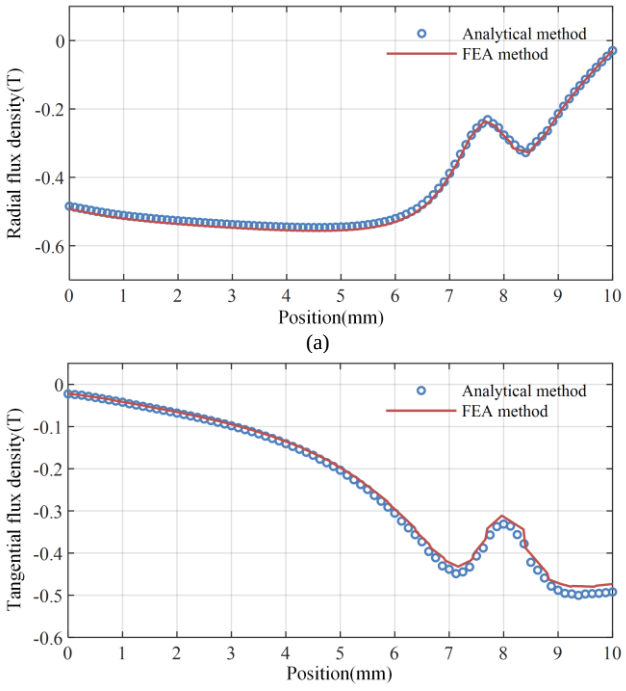

Fig. 15. Magnetic density distribution of the auxiliary teeth region
(a) Radial magnetic density distribution
(b) Tangential magnetic density distribution

Fig. 15 compares the analytically predicted and FEM-calculated magnetic flux density distributions of the auxiliary teeth region. Good agreement is achieved. The radial flux density max value in the auxiliary teeth region is slightly larger than that in the end region, which is approximately 0.52 T. The tangential flux density value ranges from 0.02 T to 0.48 T. The small discrepancy may be attributed to the maximum harmonic order in the analytical model.

The distribution of magnetic flux density in the entire slot region is given in Fig. 16. The analytical solutions agree with the FEM results with good accuracy. The small difference is due to the different relative permeabilities of each location in the slot area.

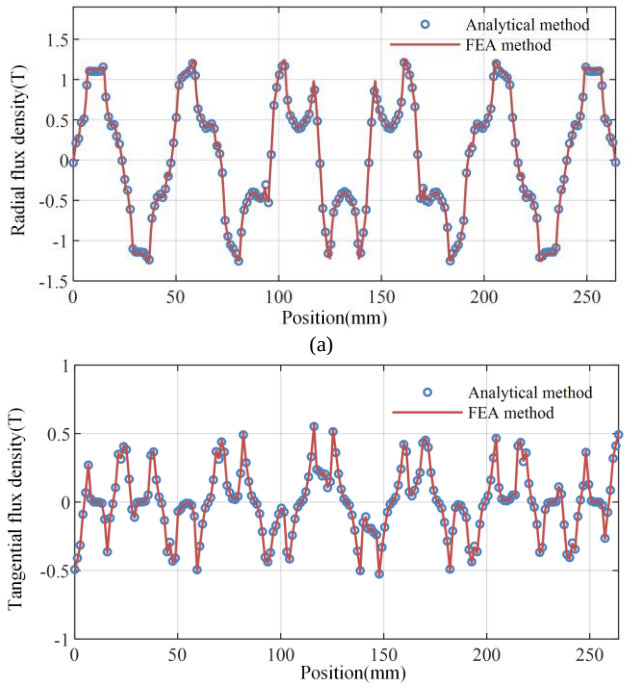

Fig. 16. Magnetic density distribution of the whole teeth region
(a) Radial magnetic density distribution
(b) Tangential magnetic density distribution

Fig. 17 compares the analytical results and FEM calculated armature reaction field of the air gap region for a given position. Excellent agreement is achieved, the main discrepancy being attributable to the harmonic order of SD and crowding effect of SC mapping. In addition, the proposed array lies in the axially magnetized PM based on the Halbach PM array, thus, the comparison between proposed array and Halbach array is conducted under the condition of the same permanent magnet volume, the results are also given in Fig. 17. From the Fig. 17, it can be found that the radial flux density amplitude of proposed PM array is about 1.2 T, the traditional Halbach PM array is about 0.8 T, and the tangential flux density of Halbach array is also slightly lower than T-type array, thus, the proposed PM array achieves obvious flux density enhancement can be verified.

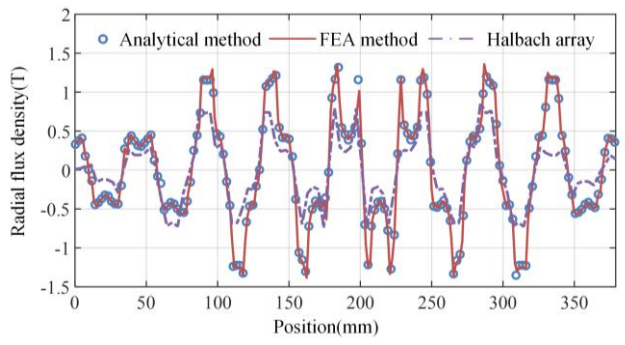

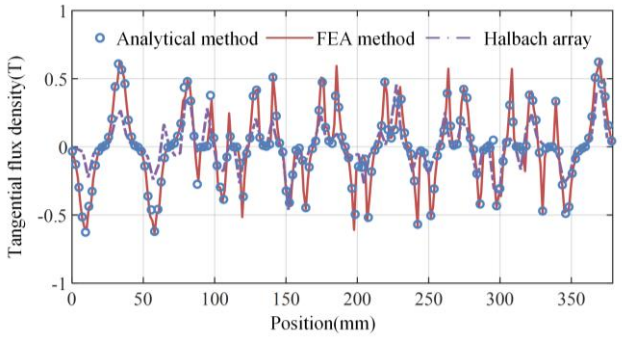

(b)

Fig. 17. Magnetic density distribution of the air gap region
(a) Radial magnetic density distribution
(b) Tangential magnetic density distribution

The distribution of the back-EMF in the A phase is shown in Fig. 18. The analytical results match well with FEM. And from Fig. 18, the back-EMF of the proposed linear machine is higher than that of Halbach PM array which caused by the increased magnetic flux makes the flux linkage larger and induces higher electromotive force. Meanwhile, it should be noted that the back-EMF is not sinusoidal, it is mainly because the linear machine is not running at a uniform speed, the speed is set to the form of a cos function to simulate oscillatory operation, and the oscillating stroke is smaller than the pole pitch. When the mover of the T-TPMLM moves to the vicinity of the balance position, a large amplitude and high-frequency signal is induced in the stator coil. When the mover back to the upper or lower end position, the relative velocity between the stator and the mover is small, inducing a small output voltage at a low frequency in the stator coil.

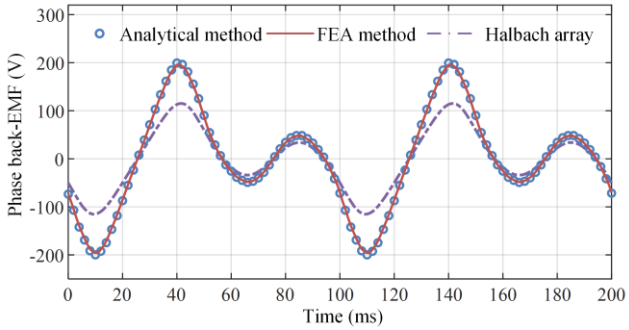

Fig. 18. Phase back-EMF distribution of the proposed linear machine

A comparison between the thrust forces predicted by the analytical method and FEM is given in Fig. 19 (a). The analytical results are close to the FEM results, the small discrepancy in the predictions between two methods is mainly attributed to the assumption that the iron permeability is infinite, and that the magnetic pressure drop in the iron is neglected, thus producing an amplitude discrepancy in the thrust force distribution. At the same time, from Fig. 19(a), it can be seen that the thrust force of T-type array is 2.5 times higher than the proposed linear machine, the main reason is that due to the flux concentration effect, the proposed T-type array has an obvious flux increase in the coil region, and the total thrust force generated by coils in the air gap is the combined effect of magnetic flux density in the whole area occupied by the coils, so the thrust force can be enhanced. Meanwhile, high fundamental harmonic amplitudes of thrust force can be achieved base on this effect, the harmonic spectra distribution of thrust forces of two investigated machines is presented in Fig. 19 (b). The amplitude of T-type array is significantly higher than that of Halbach PM array.

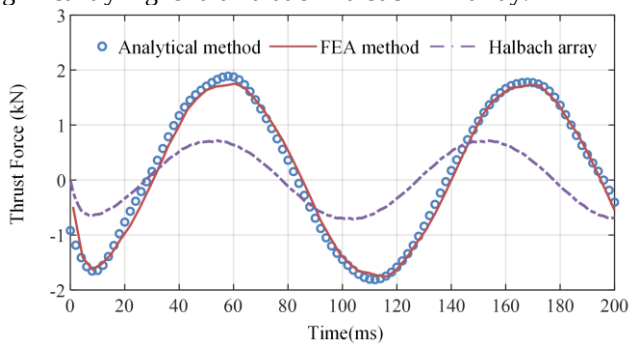

(a)

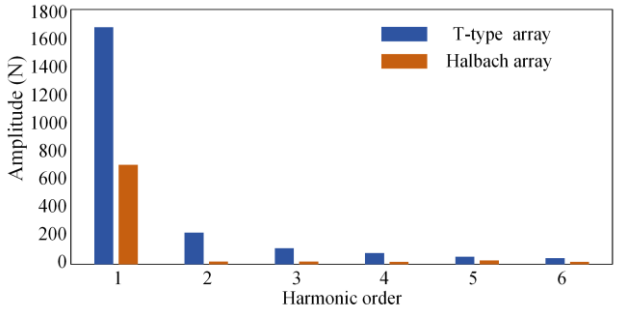

(b)

Fig. 19. Thrust force and Harmonic spectra of the T-TPMLM
(a) Thrust force distribution of the T-TPMLM
(b) Harmonic spectra distribution of the T-TPMLM

B. Electromagnetic Performance Comparison of Three different types of Linear machines

To confirm the superiority of the proposed T-TPMLM, its electromagnetic performance is compared with a traditional radial magnetization tubular linear machine (RSM-TPMLM) and a Halbach magnetization tubular linear machine (Hal-TPMLM) when they are running in generation mode. For fair comparison, all the linear machines were optimized, and share the same 12 slot/11 pole, winding configuration, identical volume, shaft length, speed, slot filling factor, and material properties. The main parameters of the three investigated linear machines are listed in Table I.

TABLE I
MAIN PARAMETERS CONFIGURATIONS OF THREE TYPE LINEAR MACHINES

Parameter	T-TPMLM	RSM-TPMLM	Hal-TPMLM
Axial length of primary, L_s		281 mm	
Length of the mover, L_i		379 mm	
Width of Slot, L_{sw}		6.75 mm	
Width of teeth, L_t		8.5 mm	
Height of stator, h_s		34 mm	
Out radius of stator, R_o		120 mm	
Pole pitch, τ_p		24 mm	
Length of air-gap, g		1 mm	
Length of PM, L_{pm_R} (Radial magnetization)		19 mm	
Thickness of PM, h_{m_R} (Radial magnetization)	3 mm	5 mm	4 mm
Thickness of PM, h_{m_a} (Axial magnetization)	3 mm	--	5 mm
Length of PM, L_{pm_R} (Axial magnetization)	17 mm	--	4 mm
Inner Radius of mover, R_i	68 mm	70 mm	
PM volume (m^3)	8.46×10^{-4}	7.88×10^{-4}	9.43×10^{-4}

Number of coils, N_c	85
Magnet grade	NdFe35
Steel grade	DW470

In Figs. 20-22, the no-load performances of the proposed T-TPMLM, RSM-TPMLM, and Hal-TPMLM are compared. Fig. 20 shows that the magnetic flux hinged by the T-TPMLM is approximately 2.6 Wb, while that of the traditional RSM-TPMLM and Hal-TPMLM are approximately 2.3 Wb and 2.4 Wb respectively, which indicates a significant improvement in the magnetization effect of the proposed linear machine.

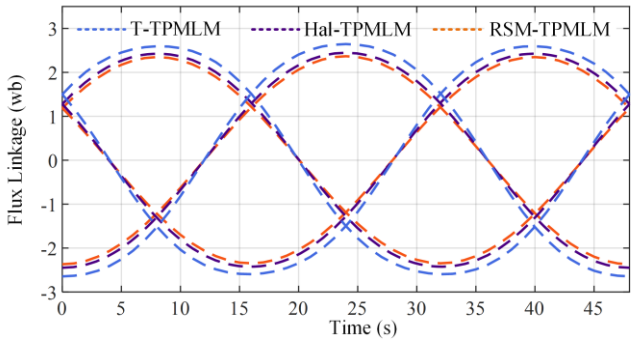

Fig. 20. Comparison the flux linkage distribution of three linear machines

Fig. 21 shows the comparative distribution of the back-EMF under open-circuit conditions when three linear machines operate at the same oscillating speed. From Fig. 21, the maximum voltage of the RSM-TPMLM, Hal-TPMLM and T-TPMLM are 197.86 V, 215.61 V, and 261.79 V. However, in Fig. 22, the peak-to-peak value of the detent force in the proposed T-TPMLM is a litter higher, which is mainly caused by the concentration effect makes the magnetic flux density increased, and magnetic flux density always changes for different air gap positions, while the total force is the combined effect of magnetic flux density in the whole area occupied by the coils, thus, the force become larger.

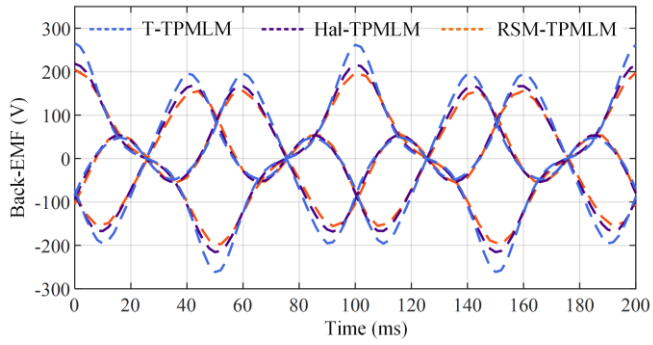

Fig. 21. Comparison the back-emf distribution of three linear machines

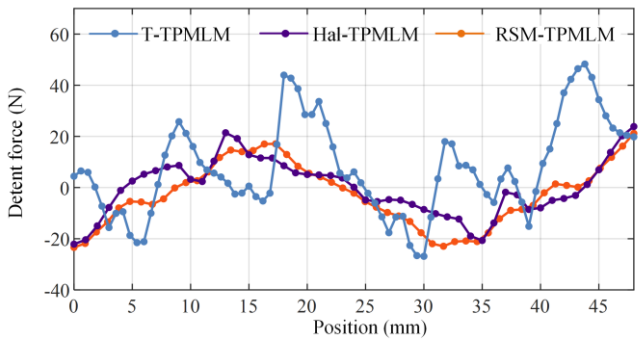

Fig. 22. Comparison the detent force of three linear machines

Fig. 23 presents the output voltage and current maximum value comparison of three linear machines at various load and same frequency conditions. It can be observed that with the load increases, the output voltage increases, and the current decreases. When they operate at load R=50 Ω, the T-TPMLM maximum output voltage of phase B is about 219 V which has nearly 42% and 30% higher than the RSM-TPMLM and Hal-TPMLM. At the same time, the output current of the proposed T-TPMLM was approximately 20% greater than that of two conventional SM-TPMLM.

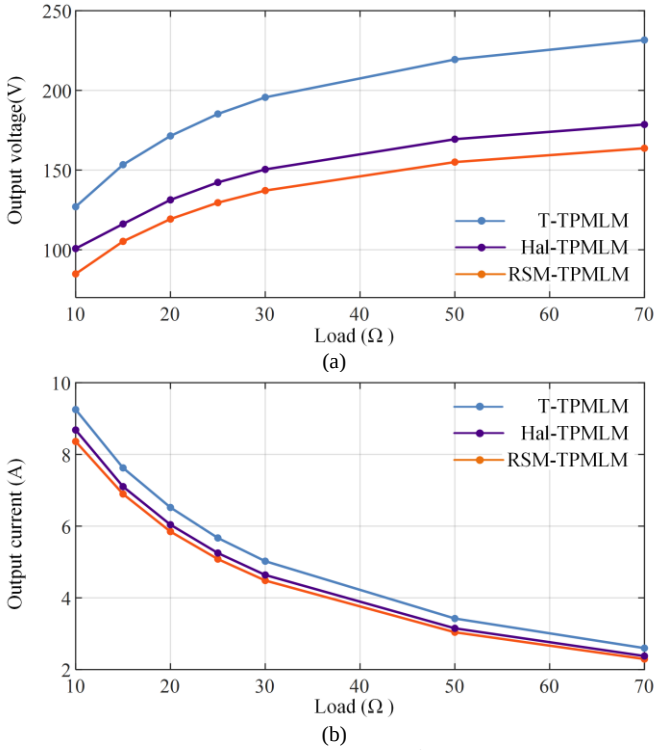

Fig. 23 Output voltage and current comparison of three linear machines
(a) Comparison the output voltage with various load
(b) Comparison the output current with various load

The power and efficiency of the proposed T-TPMLM, RSM-TPMLM, and Hal-TPMLM are compared in Fig. 24. With increasing the load, the output power of the linear machine decreases, while the efficiency changes in the opposite trend, gradually increasing. The maximum output power of the T-TPMLM is 714 W, approximately 1.2 times and 1.1 times than that of the RSM-TPMLM and Hal-TPMLM. When the load is at 50 Ω, the T-TPMLM efficiency is approximately 85%, which is improved by about 2%.

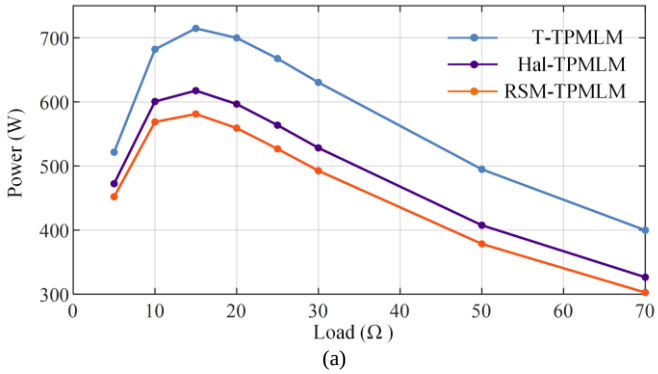

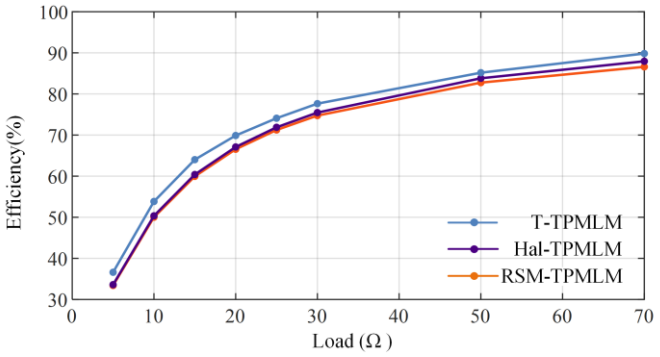

(b)

Fig. 24. Power and efficiency comparison of three linear machine
(a) Comparison the power value with various load
(b) Comparison the efficiency value with various load

The loss calculation of the three linear machines under the same power conditions are compared and given in Table II. The proposed T-TPMLM copper loss and PM loss are lower than that of two traditional linear machines, owing to the less copper and PM consumption, while the iron loss is little higher because its strong armature reaction effect and the embedded structure causes higher iron usage. Finally, only taking the copper loss, core loss, and PM loss into consideration, the total loss of proposed linear machine is lower, thus, it provides the high efficiency.

In addition, the material usage of three linear machines is given, due to the PM cost occupies the largest proportion of the permanent magnet linear machine, therefore, the PM usage can reflect the machine cost, and the power density can explain the energy conversion ability of the air gap machine for three linear machines which are also presented in Table II.

Overall take the power, loss, efficiency, power density, thrust ripple and main component usage in to considerations, the radar map of three linear machines is plotted in Fig 25. It can be seen the proposed T-TPMLM has a good electromagnetic performance.

TABLE II
COMPARISON OF THE THREE LINEAR MACHINES

Item	T-TPMLM	RSM-TPMLM	HAL-TPMLM
Power (W)	500	500	500
Copper loss (W)	71.14	122.13	92.97
Iron loss (W)	6.13	5.31	5.18
Magnet loss (W)	1.56	1.74	1.67
Total loss (W)	78.83	129.18	99.82
Copper usage (m^3)	2.5×10^{-3}	3.3×10^{-3}	2.9×10^{-3}
PM usage (m^3)	8.41×10^{-4}	11.01×10^{-4}	9.74×10^{-4}
Back-Iron usage (m^3)	2.44×10^{-3}	1.85×10^{-3}	1.77×10^{-3}
Power density (W/ kg)	13.15	11.09	12.14

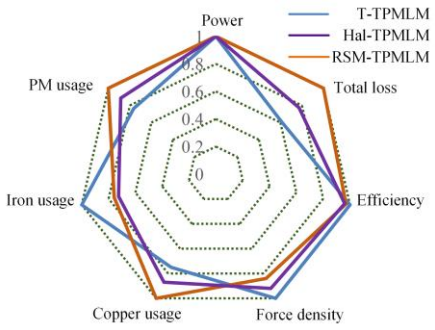

Fig. 25. Overall comparison of three linear machines

Besides, considering the special application of the linear machine, the PM mechanical structure strength of these three linear machines is analysed as shown in Fig. 26. From Fig. 26(a) it can be found that the PMs equivalent stress of traditional RSM-TPMLM range from 1476.2 Pa to 4.38×10^5 Pa, the average equivalent stress is about 70614 Pa, and the Hal-TPMLM range from 1455 Pa to 4.17×10^5 Pa, the average equivalent stress is about 70078 Pa. However, the proposed T-TPMLM PM equivalent stress is from 12.89 Pa to 3.68×10^5 Pa, the average equivalent stress is about 33640 Pa, which improved the mechanical structure and prevent the PM to fall off.

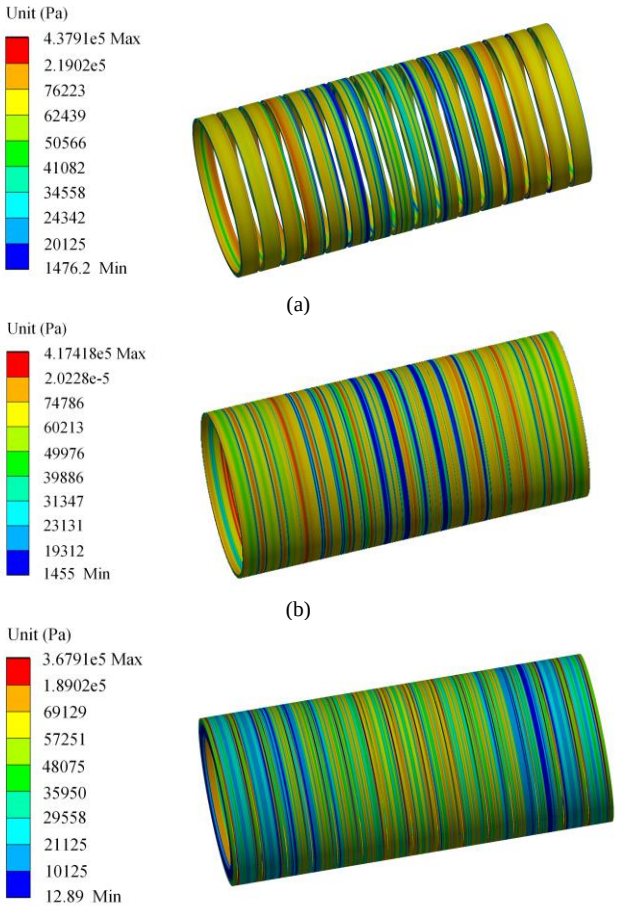

Fig. 26. PM mechanical structure strength comparison of three linear machines
(a) Equivalent stress distribution of RSM-TPMLM
(b) Equivalent stress distribution of Hal-TPMLM
(c) Equivalent stress distribution of T-TPMLM

C. *Experimental validation*

To further validate the accuracy of analytical model and the merit performances of the proposed T-TPMLM, a prototype is manufactured based on the parameters in Table I. During processing, the moving iron core is assembled with circular iron blocks, and each iron block is embedded with corresponding axial and radial magnetized fan-shaped permanent magnets. To ensure reliable adhesion of the permanent magnets, a high-strength anaerobic adhesive is used for bonding between the permanent magnets and the circular iron core, all the iron blocks are placed on the aluminium alloy cylinder for fixation, the mover of T-type

magnet array as shown in Fig. 27 (a), and the stator uses the lamination process, which is made of 0.5 mm silicon steel sheet as shown in Fig. 27(b). The size of the gap between the stator and mover is determined by the linear bearing, the electromagnetic experimental platform is shown in Fig. 27(c). The linear reciprocating motion is completed by crankshaft connecting device. The no-load experiment is tested by adjusting the power supply frequency of the rotating motor, the linear machine can be tested at different speeds. The on-load experiment requires multi-pole resistance modules to be connected to the output of the linear machine to facilitate the measurement of parameters such as output voltage, current and power under various load conditions. Besides, the test platform for measuring the detent force is given in Fig. 27(b), the force test device is coaxial connected with the prototype, the linear slide table is driven by a rotary motor to obtain a constant linear motion. The tension sensor range is 0-30 kg, corresponding output voltage is 0-5 V, and the measurement accuracy is 0.03% F. S. The signal from the sensor is recorded by using an oscilloscope with manual automatic switching mode.

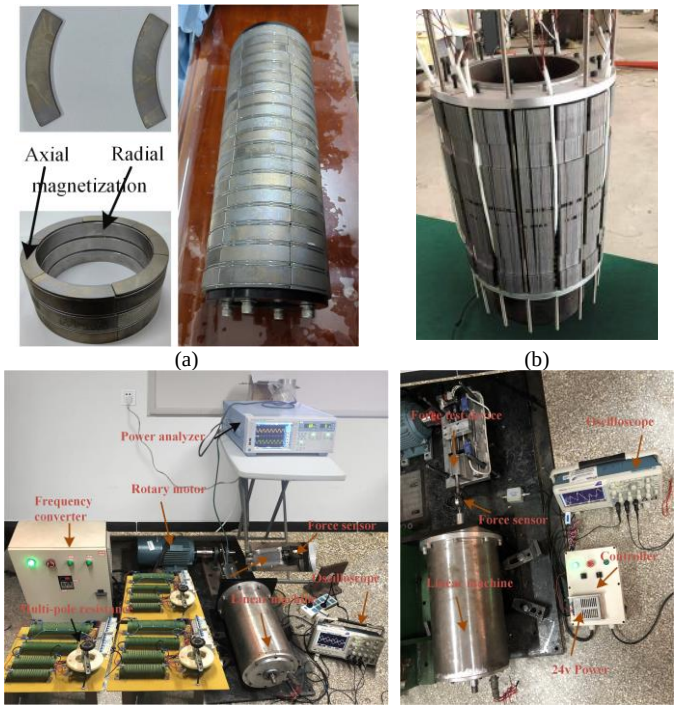

Fig. 27. Prototype and test platform of the proposed linear machine
(a) T-type magnet array mover of proposed linear machine
(b) Stator of proposed linear machine
(c) Electromagnetic test platform of proposed linear machine
(d) Detent force test platform of proposed linear machine

Two operating states of the linear machine under open-circuit condition are tested. Firstly, the linear machine is running at uniform speed v=0.46 m/s, the line back-EMF waveform from the oscilloscope is shown in Fig. 28 (a) and compared with FEA in Fig. 28(b), a good agreement can be achieved. Then, to better simulate the linear machine oscillation motion for harsh environments such as ocean wave power generation, space stirling power generation. etc. The linear machines operated at reciprocating oscillation speed is set. The analytical, FEA predictions of back-emf are compared with the measured results shown in Fig. 28 (c), the maximum values are 228.7 V, 221.3 V and 204.9 V respectively. It can be observed that they are consistent with each other, which confirms the correctness of the analytical model. A phase discrepancy between predicted results and test is mainly caused by minute fluctuations in drive motor and power frequency.

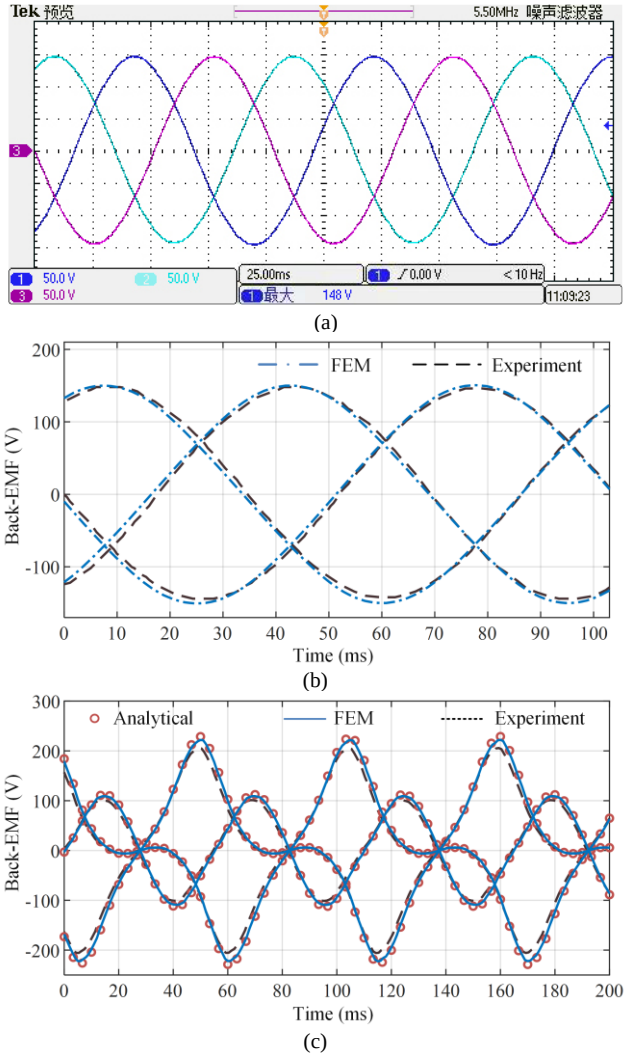

Fig. 28. Back-EMF comparison under two operating states
(a) Screenshot of line back-EMF at constant speed
(b) Back-EMF comparison between FEM and test at constant speed
(c) Back-EMF comparison between two predicted methods and test at oscillation speed

Fig. 29 gives the detent forces obtained by the analytical model, FEM and experimental at a speed of 1 mm/s. The analytical results basically agree with those results calculated by FEM and test, the error is approximately 2%. The slightly deviation is might be due to the test speed is low, the starting and stopping processes make the machine under non-quasi-static, resulting in some biases in measurement, and the mechanical tolerance are not considered in the predicted methods.

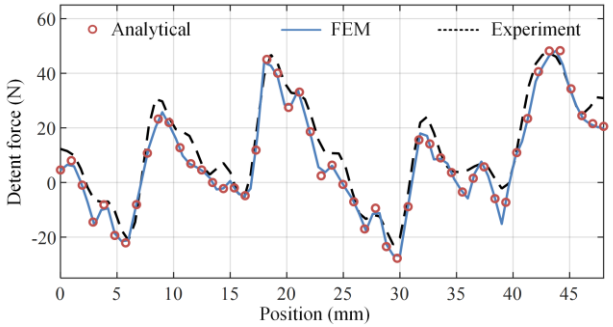

Fig. 29. Detent force comparison obtained by two predicted methods and test

The output voltage and current waveforms are compared, as presented in Fig. 30. Good agreement is obtained between predicted and measured results, the slight phase difference is mainly due to the experimental platform uses a crankshaft connecting rod to simulate sine motion, which makes the speed difference between the prime mover and the linear machine, and the strong armature reaction causes the voltage amplitude to drop slightly.

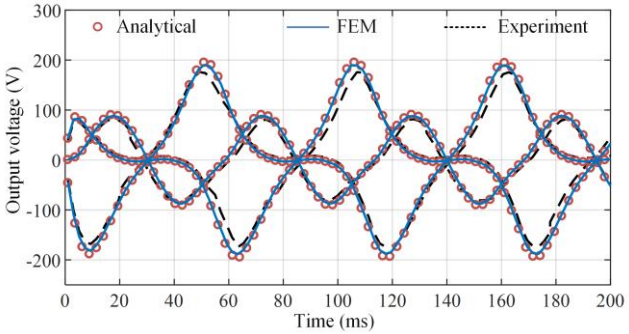

Fig. 30. Comparison of the output voltage between two predicted methods and test under load conditions at R=50 Ω

Fig. 31 presents the power various with the load. As the load decreases, the errors in the analysis, simulation and test gradually increase, because with decreasing load, the current growth, the analysis method do not consider the influence of saturation and magnetic leakage, so the results are slightly higher than the FEM, while the actual measurement of thrust force are a little lower than the two prediction methods due to the larger current make the machine temperature rises and the winding resistance increases.

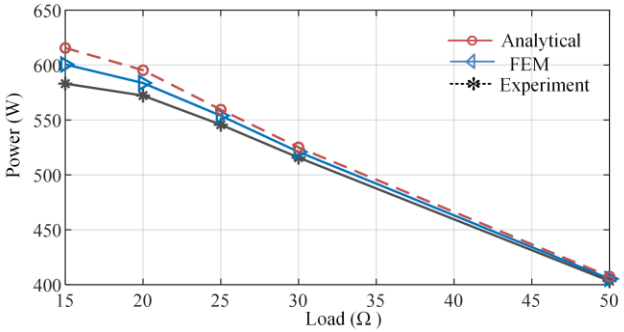

Fig. 31. Comparison of the thrust force between two predicted methods and test under different load conditions

As mentioned in [30], magnetic saturation is usually not taken into consideration in the SD method, the loss cannot be calculated accurately which is the drawback of this approach. So, in this part, the losses prediction is compared between the measured and FEM, the results are given in Fig. 32. The curve characteristics are similar, however, the FEM underestimate the losses at light loads compared with the experimental, higher current makes the eddy currents more dominant, at the same time, the vibration of the experimental platform also increases the loss value of test.

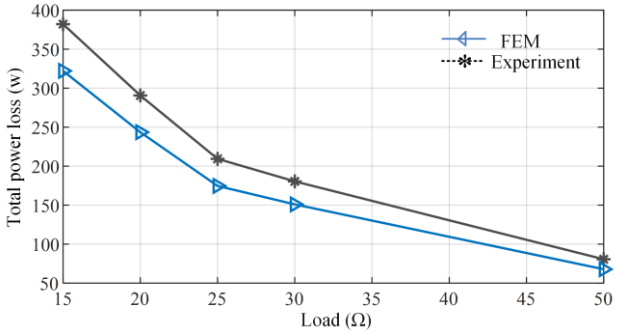

Fig. 32. Comparison of the total power loss between two predicted methods and test under different load conditions

When the rated load is R=50 Ω, the efficiency of the proposed linear machine is tested by using a power analyser. The efficiencies between FEM and measurement are given in Table III, the tested efficiency is nearly 8.8% lower than the predicted efficiency. The reason for the difference is from machining error and the bearing loss which are not considered in the calculation of the FEM.

TABLE III
EFFICIENCY COMPARISON OF TWO METHODS

Item	Value
FEM efficiency	84.72%
Tested efficiency	77.26%

V. CONCLUSION

In this paper, an improved T-type tubular permanent magnet linear machine is investigated, and the structure and operating principle of the linear machine are described. By establishing an equivalent analytical model, the magnetic field can be quickly and accurately predicted. In addition, a comprehensive comparison including electromagnetic performance and mechanical strength of three linear machines is evaluated. The conclusions are summarized as follows:

1) This paper presents a relatively accurate analysis model for determine the magnetic field distribution of the proposed T-TPMLM. The flux density distributions in the air-gap, slot regions and end area calculated with the analytical model are in close agreement with those calculated with the 2D FEM. The back-emf and thrust force with an error less than 8%. Besides, the flux concentration effect of T-type array has been proved by comparison with the same PM volume of Halbach array.

2) A quantitative electromagnetic characteristic of T-TPMLM with Hal-TPMLM and RSM-TPMLM were analysed and compared at identical volume, shaft length, speed etc. The results showed that the proposed T-TPMLM can provide nearly 17% power improvement, and 2% efficiency growth, while sacrificing 4.5% of the thrust fluctuation. Meanwhile, the paper discusses the loss and cost-effectiveness of three linear machines at the same output power condition, the proposed T-TPMLM shows at least 26% lower total loss than the other two conventional case, the iron usage of T-TPMLM

is little higher than the other machines, but the PM and copper utilization clearly decreases. The power density improved over 10%, which verify the performance advantages of proposed linear machine. In addition, the PM average equivalent stress of the proposed T-TPMLM is nearly half that of the other two linear machines, which proves that the proposed linear machine can better protect the permanent magnet from falling off.

3) A prototype of the T-TPMLM is manufactured and experimental results coincide well with the effectiveness of the analysis method and FEA predicted results. The small deviation in the phase and amplitude is mainly caused by one reason: the converter adopts a manual twist setting, and the actual frequency slight below 10Hz, which is approximately 9.2Hz. Another reason is that the crankshaft connecting the rod device makes the speed different between the driving motor and the linear machine, at the same time, as the frequency increases, mechanical vibration will also cause errors.

Overall, the proposed T-TPMLM has good performance, and the proposed analysis method can be useful for predicting the magnetic field of linear machines. However, several challenges need to be addressed and will be down in future work: 1) The proposed analysis method is applicable for the initial design stage, it has high accuracy, however, due to saturation effect is not considered, the loss calculation needs to be future explored. 2) The paper focuses on the analysis of magnetic field properties, the influence of temperature on electromagnetic properties will be presented in future work. 3) The mechanical manufacturing challenges of T-TPMLM mainly involve the design and assembly of T-type magnet arrays. In this paper, modular assembly technology is adopted by an iron block, however, this approach is useful for low-speed high-temperature applications. For high-speed applications, electromagnetic properties may be suppressed. In the future, we will consider the use of laminated assemblies in mover part and simplify the assembly process.

REFERENCES

[1] L. Guo, Q. Zhou, M. Galea, and W. Lu, "Cogging Force Optimization of Double-Sided Tubular Linear Machine with Tooth-Cutting," *IEEE Trans. Ind. Electron.*, vol. 69, no. 7, pp. 7161–7169, Jul. 2022, doi: 10.1109/TIE.2021.3101017.

[2] H. Diab, Y. Amara, G. Barakat, and M. Ghandour, "Translator Eccentricity Analysis in Tubular Linear Machines Using Quasi-3-D Finite Element Method Modeling," *IEEE Trans. Magn.*, vol. 58, no. 2, pp. 1–5, Feb. 2022, doi: 10.1109/TMAG.2021.3078399.

[3] R. Guo, H. Yu, and B. Guo, "Analysis of a Tubular Linear Permanent Magnet Oscillator With Auxiliary Teeth Configuration for Energy Conversion System," *IEEE Trans. Transp. Electrific.*, vol. 6, no. 2, pp. 602–611, Jun. 2020, doi: 10.1109/TTE.2020.2977209.

[4] L. Zhang *et al.*, "Comparison Between Dual-Armature Linear Switched Flux Permanent Magnet Machine and Linear Surface-Mounted Permanent Magnet Machine Considering Thermal Conditions," *IEEE Trans. Energy Convers.*, vol. 36, no. 4, pp. 3522–3532, Dec. 2021, doi: 10.1109/TEC.2021.3076529.

[5] C. Weissbacher, H. Stelzer, and K. Hameyer, "Application of a Tubular Linear Actuator as an Axial Magnetic Bearing," *IEEE/ASME Trans. Mechatron.*, vol. 15, no. 4, pp. 615–622, Aug. 2010, doi: 10.1109/TMECH.2009.2031111.

[6] Y. Ni, Z. Liu, B. Xiao, and Q. Wang, "Optimum Split Ratio in Surface-Mounted Permanent Magnet Machines With Pieced Halbach Magnet Array," *IEEE Trans. Energy Convers.*, vol. 35, no. 4, pp. 1877–1885, Dec. 2020, doi: 10.1109/TEC.2020.2997015.

[7] M. Shen, P.-D. Pfister, C. Tang, and Y. Fang, "A Hybrid Model of Permanent-Magnet Machines Combining Fourier Analytical Model With Finite Element Method, Taking Magnetic Saturation Into Account," *IEEE Trans. Magn.*, vol. 57, no. 2, pp. 1–5, Feb. 2021, doi: 10.1109/TMAG.2020.3005802.

[8] P. Naderi, S. Sharouni, and M. Moradzadeh, "Linear vernier machine wave converter modelling and analysis by MEC," *IET Electric Power Applications*, vol. 14, no. 5, pp. 751–761, May 2020, doi: 10.1049/iet-epa.2019.0413.

[9] H. Hu, X. Liu, J. Zhao, and Y. Guo, "Analysis and Minimization of Detent End Force in Linear Permanent Magnet Synchronous Machines," *IEEE Trans. Ind. Electron.*, vol. 65, no. 3, pp. 2475–2486, Mar. 2018, doi: 10.1109/TIE.2017.2740851.

[10] H. Hu, J. Zhao, X. Liu, Y. Guo, and J. Zhu, "No-Load Magnetic Field and Cogging Force Calculation in Linear Permanent-Magnet Synchronous Machines With Semiclosed Slots," *IEEE Trans. Ind. Electron.*, vol. 64, no. 7, pp. 5564–5575, Jul. 2017, doi: 10.1109/TIE.2016.2645509.

[11] J. Zhao, Q. Mou, C. Zhu, Z. Chen, and J. Li, "Study on a Double-Sided Permanent-Magnet Linear Synchronous Motor With Reversed Slots," *IEEE/ASME Trans. Mechatron.*, vol. 26, no. 1, pp. 3–12, Feb. 2021, doi: 10.1109/TMECH.2020.2987106.

[12] Jiabin Wang, D. Howe, and Zhengyu Lin, "Design Optimization of Short-Stroke Single-Phase Tubular Permanent-Magnet Motor for Refrigeration Applications," *IEEE Trans. Ind. Electron.*, vol. 57, no. 1, pp. 327–334, Jan. 2010, doi: 10.1109/TIE.2009.2025710.

[13] A. Souissi, M. W. Zouaghi, I. Abdennadher, and A. Masmoudi, "MEC-Based Modeling and Sizing of a Tubular Linear PM Synchronous Machine," *IEEE Trans. on Ind. Applicat.*, vol. 51, no. 3, pp. 2181–2194, May 2015, doi: 10.1109/TIA.2014.2382765.

[14] Z. Ahmad, A. Hassan, F. Khan, and I. Lazoglu, "Design of a high thrust density moving magnet linear actuator with magnetic flux bridge," *IET Electric Power Applications*, vol. 14, no. 7, pp. 1256–1262, Jul. 2020, doi: 10.1049/iet-epa.2019.0789.

[15] K.-H. Shin, H.-I. Park, J.-M. Kim, H.-W. Cho, and J.-Y. Choi, "Optimum Iron Pole Design of a Tubular Linear Synchronous Machine With Double-Sided Axially Magnetized Permanent Magnets Considering Leakage Flux," *IEEE Trans. Magn.*, vol. 52, no. 7, pp. 1–4, Jul. 2016, doi: 10.1109/TMAG.2016.2524643.

[16] K.-H. Shin, K.-H. Jung, H.-W. Cho, and J.-Y. Choi, "Analytical Modeling and Experimental Verification for Electromagnetic Analysis of Tubular Linear Synchronous Machines with Axially Magnetized Permanent Magnets and Flux-Passing Iron Poles," *IEEE Trans. Magn.*, vol. 54, no. 11, pp. 1–6, Nov. 2018, doi: 10.1109/TMAG.2018.2847410.

[17] A. Musolino, M. Raugi, R. Rizzo, and L. Sani, "A Semi-Anaytical Model for the Analysis of a Permanent Magnet Tubular Linear Generator," *IEEE Trans. on Ind. Applicat.*, vol. 54, no. 1, pp. 204–212, Jan. 2018, doi: 10.1109/TIA.2017.2756868.

[18] J. Wang, D. Howe, and G. W. Jewell, "Analysis and Design Optimization of an Improved Axially Magnetized Tubular Permanent-Magnet Machine," *IEEE Trans. On Energy Conversion*, vol. 19, no. 2, pp. 289–295, Jun. 2004, doi: 10.1109/TEC.2004.827026.

[19] W.-J. Kim, M. T. Berhan, D. L. Trumper, and J. H. Lang, "Analysis and implementation of a tubular motor with Halbach magnet array," in *IAS '96. Conference Record of the 1996 IEEE Industry Applications Conference Thirty-First IAS Annual Meeting*, San Diego, CA, USA, 1996, vol. 1, pp. 471–478. doi: 10.1109/IAS.1996.557069.

[20] M. T. Berhan, "Implementation of a Halbach array in a tubular linear motor," Massachusetts Institute of Technology, 1996.

[21] Z. Liao, J. Yue, and G. Lin, "Application Research of HTS Linear Motor Based on Halbach Array in High Speed Maglev System," *IEEE Trans. Appl. Supercond.*, vol. 31, no. 5, pp. 1–7, Aug. 2021, doi: 10.1109/TASC.2021.3057836.

[22] H. Zhang, M. Yang, Y. Zhang, J. Tuo, S. Luo, and J. Xu, "Analytical field model of segmented Halbach array permanent magnet machines considering iron nonlinearity," *IET Electric Power Appl*, vol. 15, no. 6, pp. 717–727, Jun. 2021, doi: 10.1049/elp2.12069.

[23] V. Consolo, A. Musolino, R. Rizzo, and L. Sani, "Design of a Dual Halbach Array Tubular Linear Motor for Long Stroke and Large Force," in *2020 International Conference on Electrical Machines (ICEM)*, Gothenburg, Sweden, Aug. 2020, pp. 647–653. doi: 10.1109/ICEM49940.2020.9270700.

[24] D. Howe, Z. Lin, and J. Wang, "Analysis of a short-stroke, single-phase, quasi-Halbach magnetised tubular permanent magnet motor for linear compressor applications," *IET Electric Power Applications*, vol. 2, no. 3, pp. 193–200, May 2008, doi: 10.1049/iet-epa:20070281.

[25] J. Wang and D. Howe, "Analysis of axially magnetised, iron-cored, tubular permanent magnet machines," *IEE Proc., Electr. Power Appl.*, vol. 151, no. 2, p. 144, 2004, doi: 10.1049/ip-epa:20040026.

[26] Jiabin Wang, D. Howe, and G. W. Jewell, "Fringing in tubular permanent-magnet machines: part I. magnetic field distribution, flux linkage, and thrust force," *IEEE Trans. Magn.*, vol. 39, no. 6, pp. 3507–3516, Nov. 2003, doi: 10.1109/TMAG.2003.819463.

[27] Jiabin Wang and D. Howe, "Tubular modular permanent-magnet machines equipped with quasi-Halbach magnetized magnets-part II: armature reaction and design optimization," *IEEE Trans. Magn.*, vol. 41, no. 9, pp. 2479–2489, Sep. 2005, doi: 10.1109/TMAG.2005.854327.

[28] Q. Lu, B. Wu, Y. Yao, Y. Shen, and Q. Jiang, "Analytical Model of Permanent Magnet Linear Synchronous Machines Considering End Effect and Slotting Effect," *IEEE Trans. Energy Convers.*, vol. 35, no. 1, pp. 139–148, Mar. 2020, doi: 10.1109/TEC.2019.2946278.

[29] R. Guo, H. Yu, T. Xia, Z. Shi, W. Zhong, and X. Liu, "A Simplified Subdomain Analytical Model for the Design and Analysis of a Tubular Linear Permanent Magnet Oscillation Generator," *IEEE Access*, vol. 6, pp. 42355–42367, 2018, doi: 10.1109/ACCESS.2018.2859021.

[30] R. Huang, Z. Song, H. Zhao, and C. Liu, "Overview of Axial-Flux Machines and Modeling Methods," *IEEE Trans. Transp. Electrific.*, vol. 8, no. 2, pp. 2118–2132, Jun. 2022, doi: 10.1109/TTE.2022.3144594.